The Cryosphere Discuss., doi:10.5194/tc-2016-272, 2016
Manuscript under review for journal The Cryosphere
Published: 5 December 2016

The Cryosphere
Discussions
Open Access

Numerical homogenization of the viscoplastic behavior of snow based on X-ray tomography images

Antoine Wautier[1,2,3,4,5], Christian Geindreau[1], and Frédéric Flin[2]

[1]Université Grenoble Alpes, CNRS, G-INP, Laboratoire 3SR UMR5521, F-38000 Grenoble, France
[2]Météo-France – CNRS, CNRM-GAME UMR 3589, CEN, F-38400 Saint Martin d'Hères, France
[3]Now at AgroParisTech-ENGREF, 19 avenue du Maine, 75732 Paris, France.
[4]Now at Irstea UR RECOVER, 3275 Rte Cézanne, CS 40061, 13182 Aix-en-Provence Cedex 5, France.
[5]Now at Université Grenoble Alpes, Irstea, UR ETGR, 2 rue de la Papeterie-BP 76, F-38402 St-Martin-d'Hères, France.

Correspondence to: A. Wautier (antoine.wautier@gmail.com)

Abstract. The homogenization techniques recently developed for the numerical study of the elastic behavior of snow are adapted to its non-linear visco-plastic behavior. Based on the definition of kinematically uniform boundary conditions, homogenization problems are applied to 3D-images obtained by X-ray tomography, and the mechanical response of snow samples of different densities is explored. An original post-processing approach in terms of viscous dissipated powers is defined in order to formulate the macroscopic behavior of snow. Then, the ability of Abouaf models to account for snow visco-plastic behavior is shown and a homogenized constitutive equation is proposed based on a density parametrization. Finally, the mechanical responses of snow for classical laboratory tests are analyzed and compared with the proposed model.

1 Introduction

It is now well known that the macroscopic mechanical behavior of snow strongly depends on its microstructure, which is mainly characterized by its density (Mellor, 1974) and its topology (Shapiro et al., 1997), by the mechanical behavior of the ice matrix (elastic, visco-plastic, brittle-failure) depending on the external load, by the temperature (Schweizer and Camponovo, 2002) and the applied strain rate (Schulson et al., 2009). For example, at high strain rate, large deformations of snow are mainly controlled by grain rearrangements resulting from the failure of cohesive bonds, whereas at very low strain rates ($< 10^{-5}\mathrm{s}^{-1}$ typically), snow exhibits a visco-plastic behavior (Narita, 1984; Salm, 1982) which plays an important role in the long-term densification of the snowpack. In practice, a good knowledge of the macroscopic mechanical behavior of snow in a wide range of applied loads, strain rates and temperatures is of a particular interest with respect to avalanche risk forecasting or to determine the forces on avalanche defense structures.

During the last decades, numerous experimental studies have been performed in order to characterize the macroscopic behavior of different types of snow under various loading conditions and temperatures (Mellor, 1974; Salm, 1982; Desrues et al., 1980; Shapiro et al., 1997; Bartelt and von Moos, 2000; Moos et al., 2003; Scopozza and Bartelt, 2003a). In the framework of the continuum mechanics, several models have been then proposed in order to reflect these experimental data (Desrues et al., 1980; Scopozza and Bartelt, 2003b; Cresseri and Jommi, 2005; Navarre et al., 2007; Cresseri et al., 2009). However, the fitted material parameters arising in these models often characterize the mean properties of a few types of snow in a restricted density range. Thanks to the recent application of X-ray tomography to snow (Brzoska et al., 1999; Schneebeli, 2004; Kaempfer et al., 2005; Flin and Brzoska, 2008; Chen and Baker, 2010; Srivastava et al., 2010; Pinzer et al., 2012; Wang and Baker, 2013; Adams and Walters, 2014; Calonne et al., 2015) good databases of 3D images for the different snow types described in the international classification (Fierz et al., 2009) are now available (Calonne et al., 2012; Löwe et al., 2013). Given these extensive geometrical descriptions of snow, its corresponding macroscopic behavior can be up-scaled in a more systematic way thanks to the use of techniques derived from the homogenization theory (Dormieux and Bourgeois, 2002; Auriault et al., 2010).

In recent works, the combination of X-ray tomography imaging, finite elements techniques or discrete element methods (DEM) and ever increasing computing power was used to bridge the gap between the topology of the ice skeleton of snow and its mechanical behavior. If discrete element methods are well suited to model deformations resulting from grain rearrangement and grain bound breakage (Hagenmuller et al., 2015), finite element modeling is more adapted to account for the deformation of the ice skeleton. This last method is thus well-suited to the long term compaction of the snowpack under its own weight coming from the ice viscosity. However, most of the studies only considered the elastic behavior of snow so far (Schneebeli, 2004; Pieritz et al., 2004; Srivastava et al., 2010; Köchle and Schneebeli, 2014; Wautier et al., 2015; Srivastava et al., 2016), possibly up to a brittle failure (Hagenmuller et al., 2014). Concerning the modeling of more complex snow constitutive behaviors, the proposed approaches mainly focus on the modeling of uniaxial compression tests. For instance, Theile et al. (2011) proposed a beam network model based on 3D images to simulate creep of snow, Chandel et al. (2014) used an elasto-plastic constitutive law for ice, Schleef et al. (2014) considered the viscous behavior of snow in the case of uniaxial compression tests followed by a relaxation phase.

In the present work, we propose to determine the 3D macroscopic viscoplastic constitutive law of snow in the wake of the homogenization approach performed in Wautier et al. (2015) within the framework of elasticity. For that purpose, typical kinematically uniform boundary conditions (KUBC) are applied to 3D images of snow, and finite element simulations are run in order to link the macroscopic stress response of different snow samples to imposed strain rates. The viscous mechanical behavior of ice is described by a power law of exponent n as in Theile et al. (2011). Due to the non-linear behavior under consideration, the homogenization does not provide the complete structure of the macroscopic constitutive equation (Auriault et al., 1992, 2002; Geindreau and Auriault, 1999; Orgéas et al., 2007). However, it can be shown that the exponent n is preserved at the macroscopic scale and the macroscopic dissipation potential is the volume-averaged of the local dissipation one (Suquet, 1993). Using these properties, the macroscopic constitutive equation of snow can be formulated within the framework defined by the theory of tensor function representation and by using macroscopic isodissipation surfaces (Green, 1972; Abouaf, 1985; Geindreau et al., 1999b; Orgéas et al., 2007).

The paper is organized as follow. In section 2, the numerical homogenization procedure used in Wautier et al. (2015) is recalled and adapted to the study of a non-linear constitutive equation. The section 3 presents the post-processing procedure that was used in order to characterize the macroscopic viscous behavior of snow in terms of macroscopic isodissipation curves. In section 4, the obtained numerical results for snow samples of different densities are presented and the ability of an Abouaf's model (Abouaf, 1985) to describe the macroscopic viscous behavior of snow is highlighted. Finally, in section 5, the mechanical responses of snow for classical experimental tests (uniaxial, oedometric and triaxial compression tests) are analysed and compared using the proposed model.

2 Numerical homogenization procedure: from image to macroscopic mechanical response

Based on the homogenization theory, it is often possible to replace a heterogeneous material by an equivalent homogeneous one provided that its microstructure is sufficiently small with respect to the macroscopic scale of interest. With respect to snow, this separation of scale hypothesis is satisfied in most of the cases and its macroscopic mechanical behavior can be deduced from mesovolumes obtained thanks to X-ray tomography. Previous studies showed that in most of the cases, samples of a few centimeters can be considered as representative elementary volumes (REV) for the study of the mechanical behavior of snow (Wautier et al., 2015; Srivastava et al., 2016).

Irrespective of the size of the sample considered, the boundary conditions used in an homogenization procedure introduces undesired boundary effects of varying thickness. Depending on the type of boundary conditions used, the size of the REV should be adapted accordingly. Three particular types of boundary conditions are considered to give relatively small REV. In decreasing order of REV (Kanit et al., 2003), these are statically uniform boundary conditions (SUBC), with a macroscopic homogeneous stress imposed on the boundary, kinematically uniform boundary conditions (KUBC), with a macroscopic homogeneous strain imposed on the boundary, and periodic boundary conditions (PBC), with a periodicity condition imposed on the displacement field and the normal stress across the sample boundaries. Although PBC are considered to give the best convergence with respect to the size of the REV (Kanit et al., 2003), their application to a non-periodic highly porous microstructure is not straightforward. It is necessary, for example, to enclose the sample by a virtual boundary or assume that the pores are filled by a soft material. In order to avoid the introduction of such artefacts, KUBC were retained as in Wautier et al. (2015). The KUBC numerical homogenization procedure introduced in Wautier et al. (2015) is used in this paper and easily adapted to the study of the elasto-viscoplastic behavior of snow. It consists in the four steps recalled in Fig. 1.

The first two steps remain unchanged and consist in: (i) meshing of 3D-microtomographic images (Step 1), (ii) defining the kinematic relation $\boldsymbol{u} = \mathbf{E}\cdot\boldsymbol{x}$ between the homogeneous macroscopic strain $\mathbf{E}$ and the displacement field $\boldsymbol{u}$ on the boundary (Step 2). Step 1 requires the use of the MATLAB open-source toolbox iso2mesh (Fang and Boas, 2009) while step 2 is achieved thanks to the use of the plug-in Homtools (Lejeunes et al., 2011). More details can be found in Wautier et al. (2015). The next two steps are modified in order to take into account the change in the constitutive modeling of ice.

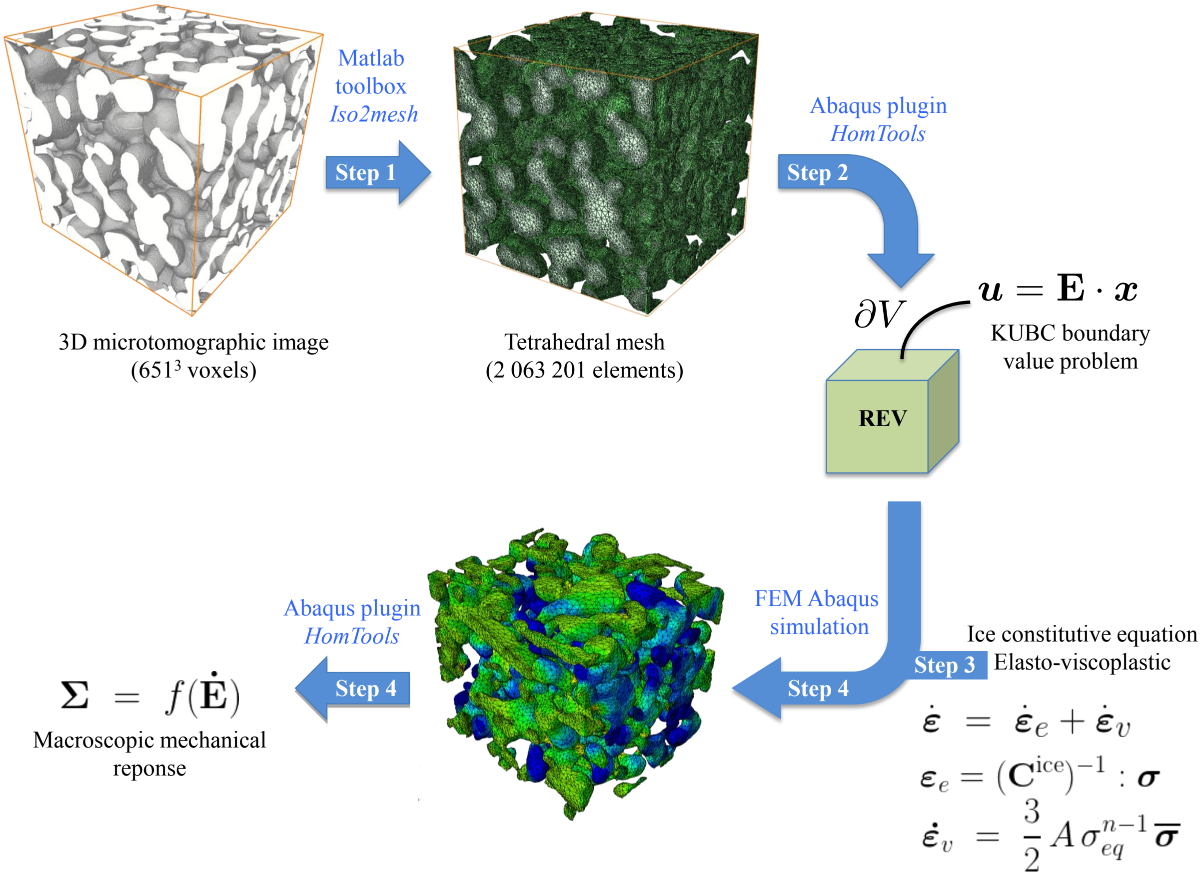

Figure 1. Four-step procedure used in order to transform 3-D microtomograph images of snow into finite element models and numerically solve KUBC homogenization boundary value problems.

2.1 Elasto-viscoplastic behavior of ice (Step 3)

In the following, the mechanical behavior of the polycrystalline ice is supposed to be elasto-viscoplastic and isotropic. The total strain rate tensor ($\dot{\boldsymbol{\varepsilon}}$) is decomposed as the sum of the elastic part ($\dot{\boldsymbol{\varepsilon}}_e$) and a viscous part ($\dot{\boldsymbol{\varepsilon}}_v$) as

$$\dot{\boldsymbol{\varepsilon}} = \dot{\boldsymbol{\varepsilon}}_e + \dot{\boldsymbol{\varepsilon}}_v. \tag{1}$$

The elastic part can be expressed as, $\boldsymbol{\varepsilon}_e = (\mathbf{C}^{\text{ice}})^{-1} : \boldsymbol{\sigma}$, where $\mathbf{C}^{\text{ice}}$ is the elastic stiffness tensor, $\boldsymbol{\sigma}$ is the Cauchy stress tensor and ":" the double contraction product. Due to isotropy, $\mathbf{C}^{\text{ice}}$ is fully defined by a Young's modulus E and a Poisson ratio ν. Concerning the viscous part, at low strain rates, the non linear mechanical behavior of ice is usually described by a power law (Mellor, 1974; Schulson et al., 2009), i.e. the Norton Hoff law in 3D (Lemaitre and Chaboche, 1985). Thus, we have

$$\dot{\boldsymbol{\varepsilon}}_v = \frac{3}{2} A \sigma_{\text{eq}}^{(n-1)} \overline{\boldsymbol{\sigma}}, \tag{2}$$

where A and n are two material parameters (which usually depend on the temperature), $\overline{\boldsymbol{\sigma}}$ is the deviatoric stress tensor and $\sigma_{\mathrm{eq}}(\boldsymbol{\sigma})$ is the equivalent stress defined as

$$\sigma_{\mathrm{eq}}(\boldsymbol{\sigma}) = \sqrt{\frac{3}{2}\overline{\boldsymbol{\sigma}}:\overline{\boldsymbol{\sigma}}} = \sqrt{\frac{3}{2}}\bar{s}_2, \qquad \overline{\boldsymbol{\sigma}} = \boldsymbol{\sigma} - \frac{1}{3}\mathrm{Tr}(\boldsymbol{\sigma})\mathbf{I}, \tag{3}$$

where $\mathbf{I}$ is the second order identity tensor, Tr is the trace operator and $\bar{s}_2$ is the second invariant of $\overline{\boldsymbol{\sigma}}$. It can be shown (Lemaitre and Chaboche, 1985) that the viscous strain rate tensor $\dot{\boldsymbol{\varepsilon}}_v$ derives from a viscous potential $\omega(\boldsymbol{\sigma})$ as

$$\dot{\boldsymbol{\varepsilon}}_v = \frac{\partial\omega}{\partial\boldsymbol{\sigma}} = \frac{\mathrm{d}\omega}{\mathrm{d}\sigma_{\mathrm{eq}}}\frac{\partial\sigma_{\mathrm{eq}}}{\partial\boldsymbol{\sigma}} = \frac{3}{2}\frac{\mathrm{d}\omega}{\mathrm{d}\sigma_{\mathrm{eq}}}\frac{\overline{\boldsymbol{\sigma}}}{\sigma_{\mathrm{eq}}}, \qquad \text{with} \quad \omega(\boldsymbol{\sigma}) = \frac{A}{n+1}\sigma_{\mathrm{eq}}^{(n+1)}. \tag{4}$$

From (2) and (4), one can define the equivalent strain rate $\dot{\varepsilon}_{\mathrm{eq}}(\dot{\boldsymbol{\varepsilon}}_v)$ as the dual variable of the equivalent stress σ_{eq} such that

$$\dot{\varepsilon}_{\mathrm{eq}}(\dot{\boldsymbol{\varepsilon}}_v) = \sqrt{\frac{2}{3}\dot{\overline{\boldsymbol{\varepsilon}}}_v:\dot{\overline{\boldsymbol{\varepsilon}}}_v} = \sqrt{\frac{2}{3}}\bar{e}_2, \quad \text{with} \quad \dot{\varepsilon}_{\mathrm{eq}} = A\sigma_{\mathrm{eq}}^n, \tag{5}$$

where $\bar{e}_2$ is the second invariant of the deviatoric part of $\dot{\boldsymbol{\varepsilon}}_v$.

If p_{v} stands for the volumetric mechanical dissipation, the equivalent stress and the equivalent strain rate verify

$$p_{\mathrm{v}} = \boldsymbol{\sigma}:\dot{\boldsymbol{\varepsilon}}_v = \bar{s}_2.\bar{e}_2 = \dot{\varepsilon}_{\mathrm{eq}}.\sigma_{\mathrm{eq}} = A\sigma_{\mathrm{eq}}^{(n+1)}. \tag{6}$$

At the microscopic scale, the viscoplastic deformation of ice is incompressible. Consequently the equivalent stress (resp. the equivalent strain rate) depends only on the second invariant $\bar{s}_2$ of $\overline{\boldsymbol{\sigma}}$ (resp. the second invariant $\bar{e}_2$ of $\dot{\overline{\boldsymbol{\varepsilon}}}_v$).

Overall, the ice matrix is thus modeled as an isotropic elasto-visco-plastic material in the finite element commercial software Abaqus. Let us remark, that a pure visco-plastic behavior cannot be simulated in a Lagrangian code such as Abaqus and the knowledge of the ice Young's modulus (E) and Poisson's ratio (ν) are also needed to ensure the efficiency of the numerical scheme. The values of the four material constants in this constitutive modeling, namely A, n, E and ν, were determined thanks to a uniaxial compression test on a cylinder of polycrystalline ice. The experiment was carried out at -10°C on an ice cylinder thanks to a micro-press operating in cold-room. After a first compression step realized at a constant strain rate of 2×10^{-6} s^{-1} until reaching a stress stabilization around 475 kPa, the ice viscous properties were identified thanks to a relaxation test. After 3500 s and as the axial stress was reduced by half, the ice elastic properties were deduced from the unloading of the ice cylinder at a higher strain rate of 1×10^{-3} s^{-1}. The Table 1 summarizes the parameter values used in this paper, which are consistent with the ones in the literature (Chandel et al., 2014; Schulson et al., 2009).

2.2 Macro-strain paths definition (Step 4)

Given a time dependent macroscopic strain loading $\mathbf{E}(t)$, the KUBC homogenization problem to be solved reads as

$$\left\{\begin{array}{lcll} \operatorname{div}\boldsymbol{\sigma} & = & 0 & \text{for } \boldsymbol{x}\in V \\ \boldsymbol{u} & = & \mathbf{E}(t)\cdot\boldsymbol{x} & \text{for } \boldsymbol{x}\in \partial V \\ \boldsymbol{\varepsilon} & = & \dfrac{1}{2}(\boldsymbol{\nabla}\,\boldsymbol{u} + {}^{t}\boldsymbol{\nabla}\,\boldsymbol{u}) & \text{for } \boldsymbol{x}\in V \\ \boldsymbol{\varepsilon} & = & \boldsymbol{\varepsilon}_e + \boldsymbol{\varepsilon}_v & \text{for } \boldsymbol{x}\in V \\ \dot{\boldsymbol{\varepsilon}}_v & = & \dfrac{3}{2}A(\boldsymbol{x})\,\sigma_{\rm eq}^{n-1}\,\overline{\boldsymbol{\sigma}} & \text{for } \boldsymbol{x}\in V \\ \boldsymbol{\sigma} & = & \dfrac{E(\boldsymbol{x})}{1+\nu}\left(\boldsymbol{\varepsilon}_e + \dfrac{\nu}{1-2\nu}\mathrm{Tr}(\boldsymbol{\varepsilon}_e)\mathbf{1}\right) & \text{for } \boldsymbol{x}\in V \end{array}\right. , \tag{7}$$

where V stands for the domain occupied by the whole snow sample and ∂V its boundary. The spatial heterogeneity of the mechanical properties of snow is captured thanks to the functions $A(\boldsymbol{x})$ and $E(\boldsymbol{x})$ defined as

$$A(\boldsymbol{x}) = \left\{\begin{array}{ll} A & \text{if } \boldsymbol{x}\in V_i \\ 0 & \text{if } \boldsymbol{x}\in V\backslash V_i \end{array}\right. \quad \text{and} \quad E(\boldsymbol{x}) = \left\{\begin{array}{ll} E & \text{if } \boldsymbol{x}\in V_i \\ 0 & \text{if } \boldsymbol{x}\in V\backslash V_i \end{array}\right. . \tag{8}$$

where $V_i \subset V$ is the domain occupied by the ice matrix. Similarly to the elastic case (Wautier et al., 2015), the macroscopic stress tensor $\boldsymbol{\Sigma}$ is deduced from the knowledge of its microscopic counterpart thanks to the volume averaging

$$\boldsymbol{\Sigma} = \frac{1}{|V|}\int_V \boldsymbol{\sigma}\,\mathrm{d}V = \langle\boldsymbol{\sigma}\rangle \tag{9}$$

As a result, for a given macroscopic strain loading $\mathbf{E}(t)$, the macroscopic stress response $\boldsymbol{\Sigma}(t)$ is recovered. The implicit function linking these two second order tensors characterizes the homogeneous behavior of the snow sample considered and can be put in the form:

$$\dot{\mathbf{E}} = \dot{\mathbf{E}}_e + \dot{\mathbf{E}}_v = \mathcal{F}(\boldsymbol{\Sigma}) \tag{10}$$

Table 1. Mechanical parameters used in the elasto-visco-plastic modeling of ice implemented in Abaqus. The values were chosen based on an experimental uniaxial compression test performed on a polycrystalline ice cylinder.

Parameters	Value
A	$1.5\ 10^{-3}\,\mathrm{MPa}^{-4.5}.\mathrm{s}^{-1}$
n	4.5
E	325 MPa
ν	0.3

where $\dot{\mathbf{E}}_e$ is the macroscopic elastic strain rate tensor and $\dot{\mathbf{E}}_v$ is the macroscopic viscous strain rate tensor. The elastic part can be expressed as, $\mathbf{E}_e = (\mathbf{C}^{\text{hom}})^{-1} : \mathbf{\Sigma}$, where $\mathbf{C}^{\text{hom}}$ is the homogenized stiffness tensor (Wautier et al., 2015). This tensor can be obtained by performing only six simulations on Representative Elementary Volumes extracted from 3D images. By contrast, the homogenization of the visco-plastic behavior requires *a priori* an infinite number of numerical simulations. However, this number of simulations can be reduced by taking into account some theoretical results (Auriault et al., 1992; Suquet, 1993; Orgéas et al., 2007). Indeed, it can be shown that:

- The homogeneity of degree n of the microscopic viscous constitutive equation (2) is preserved in the homogenization process. In other words, the macroscopic viscous strain rate $\dot{\mathbf{E}}_v$ is a homogeneous function of degree n of the macroscopic stress $\mathbf{\Sigma}$, and the macroscopic volumetric mechanical dissipation $\mathcal{P}_\text{v} = \dot{\mathbf{E}}_v : \mathbf{\Sigma}$ is an homogeneous function of degree $n+1$ of $\mathbf{\Sigma}$:

$$\left\{ \begin{array}{lcl} \dot{\mathbf{E}}_v(\lambda\mathbf{\Sigma}) & = & \lambda^n \dot{\mathbf{E}}_v(\mathbf{\Sigma}) \\ \mathcal{P}_\text{v}(\lambda\mathbf{\Sigma}) & = & \lambda\mathbf{\Sigma} : \dot{\mathbf{E}}_v(\lambda\mathbf{\Sigma}) \;=\; \lambda^{n+1}\mathcal{P}_\text{v}(\mathbf{\Sigma}) \end{array} \right. , \qquad \forall\lambda \in \mathbb{R}. \tag{11}$$

  As a result, the choice in the macroscopic strain rate $\dot{\mathbf{E}}_v$ can be reduced to the unit sphere in the second order tensor space.

- The macroscopic dissipation potential $\Omega(\mathbf{\Sigma})$ is the volume-average of the local dissipation potential ω

$$\Omega(\mathbf{\Sigma}) \;=\; \frac{1}{|V|}\int_V \omega(\boldsymbol{\sigma})\,\mathrm{d}V = \langle \omega(\boldsymbol{\sigma}) \rangle \tag{12}$$

  and consequently, as at the microscopic scale (see equation (4)), we have:

$$\dot{\mathbf{E}}_v = \frac{\partial\Omega}{\partial\mathbf{\Sigma}} = \frac{\mathrm{d}\Omega}{\mathrm{d}\Sigma_\text{eq}}\frac{\partial\Sigma_\text{eq}}{\partial\mathbf{\Sigma}}, \qquad \text{with} \quad \Omega(\mathbf{\Sigma}) = \frac{A}{n+1}\Sigma_\text{eq}^{n+1} \tag{13}$$

  where $\Sigma_\text{eq}(\mathbf{\Sigma})$ is the macroscopic equivalent stress, which verifies

$$\mathcal{P}_\text{v} = \mathbf{\Sigma} : \dot{\mathbf{E}}_v = \dot{\text{E}}_\text{eq}.\Sigma_\text{eq} = A\Sigma_\text{eq}^{n+1} \tag{14}$$

  with $\dot{\text{E}}_\text{eq}(\dot{\mathbf{E}}_v)$ the macroscopic equivalent strain rate defined by duality. As a result, the macroscopic viscoplastic law (13) is perfectly defined if the macroscopic equivalent stress Σ_eq is known. The latter equation (14) shows that this macroscopic equivalent stress Σ_eq can be fitted on iso-mechanical dissipation surfaces in the space associated with $\mathbf{\Sigma}$. In the case of general anisotropy, the form of Σ_eq can be formulated within the framework defined by the theory of representation of anisotropic tensor functions (Smith, 1971; Liu, 1982). It is also important to mention that for the ice matrix, the overall response of snow is insensitive to the sign of $\mathbf{\Sigma}$ as a consequence of definition (4). This condition may be expressed as $\Omega(\mathbf{\Sigma}) = \Omega(-\mathbf{\Sigma})$. Finally, let us remark that by definition (see (13) and (14)), the macroscopic strain rate $\dot{\mathbf{E}}_v$ is normal to iso-mechanical dissipation surfaces (normality rule).

In the following, for the sake of simplicity, we will suppose that the macroscopic viscoplastic behavior of snow is isotropic. In this particular case, it can be shown (Abouaf, 1985; Geindreau et al., 1999b; Danas et al., 2008) that the macroscopic equivalent stress is written:

$$\Sigma_{\text{eq}}(\mathbf{\Sigma}) = \Sigma_{\text{eq}}(S_1, \bar{S}_2, \bar{S}_3, \phi) \tag{15}$$

where ϕ is the snow porosity and $(S_1, \bar{S}_2, \bar{S}_3)$ are the three invariants of the macroscopic stress tensor $\mathbf{\Sigma}$ defined as:

$$S_1 \;=\; \text{Tr}(\mathbf{\Sigma}), \quad \bar{S}_2 \;=\; \sqrt{\bar{\mathbf{\Sigma}} : \bar{\mathbf{\Sigma}}}, \quad \bar{S}_3 = \det(\bar{\mathbf{\Sigma}}), \quad \text{with} \quad \bar{\mathbf{\Sigma}} = \mathbf{\Sigma} - \frac{S_1}{3}\mathbf{I}. \tag{16}$$

Similarly, the macroscopic equivalent strain rate $\dot{\text{E}}_{\text{eq}}$ takes the form:

$$\dot{\text{E}}_{\text{eq}}(\dot{\mathbf{E}}_v) = \dot{\text{E}}_{\text{eq}}(E_1, \bar{E}_2, \bar{E}_3, \phi) \tag{17}$$

where $(E_1, \bar{E}_2, \bar{E}_3)$ are the invariants of the strain rate tensor $\dot{\mathbf{E}}_v$ defined as:

$$E_1 \;=\; \text{Tr}(\dot{\mathbf{E}}_v), \quad \bar{E}_2 \;=\; \sqrt{\dot{\bar{\mathbf{E}}}_v : \dot{\bar{\mathbf{E}}}_v}, \quad \bar{E}_3 \;=\; \det(\dot{\bar{\mathbf{E}}}_v), \quad \text{with} \quad \dot{\bar{\mathbf{E}}}_v = \dot{\mathbf{E}}_v - \frac{E_1}{3}\mathbf{I}. \tag{18}$$

In contrast with the microscopic scale (see equation (3)), the macroscopic equivalent stress (15) depends on the three invariants $(S_1, \bar{S}_2, \bar{S}_3)$ of the macroscopic stress tensor $\mathbf{\Sigma}$. Indeed, at the macroscopic scale, the viscoplastic snow deformation is compressible. This compressibility, characterized by E_1, depends on the level of the mean pressure $(S_1/3)$ applied on the snow sample, as well as the mean shear stress $(\bar{S}_2)$. The third invariant $\bar{S}_3$ characterizes the loading type and is linked to the Lode angle θ in the stress space (Lemaitre and Chaboche, 1985; Danas et al., 2008):

$$\cos(3\theta) = \frac{27}{2}\frac{\bar{S}_3}{\Sigma_{\text{eq}}^3}. \tag{19}$$

As a first approximation, it seems reasonable to assume that the influence of the third invariant $\bar{S}_3$ is negligible (Green, 1972; Abouaf, 1985; Geindreau et al., 1999b; Fritzen et al., 2012). Consequently, the macroscopic volumetric mechanical dissipation $\mathcal{P}_{\text{v}}$ depends on the first and second stress and strain invariants and not only on the second ones as at the microscale (6).

$$\mathcal{P}_{\text{v}} = \mathbf{\Sigma} : \dot{\mathbf{E}}_v = \text{E}_{\text{eq}}.\Sigma_{\text{eq}} = A\Sigma_{\text{eq}}^{n+1} = \frac{1}{3}E_1.S_1 + \bar{E}_2.\bar{S}_2. \tag{20}$$

The relation (20) shows that, for a given snow porosity, the equivalent macroscopic stress Σ_{eq} can be fitted on iso-volumetric mechanical dissipation curves in the plane $(S_1/3, \bar{S}_2)$. These isodissipation curves can be obtained by plotting the values $(S_1/3, \bar{S}_2)$ corresponding to different loading conditions defined by $(E_1, \bar{E}_2)$. Therefore, the choice was made to run numerical simulation for seven diagonal strain rate tensors defined such that the loading direction in the plane $(E_1, \bar{E}_2)$ varies from 0° to 90°. More explicitly, $\dot{\mathbf{E}}$ applied on the sample is taken as

$$\dot{\mathbf{E}} \;=\; \dot{\text{E}}_{\text{ref}} \begin{pmatrix} 1 & 0 & 0 \\ 0 & \eta & 0 \\ 0 & 0 & \eta \end{pmatrix}, \tag{21}$$

with $\dot{\mathrm{E}}_{\mathrm{ref}} = 10^{-7}\,\mathrm{s}^{-1}$ and $\eta \leq 1$ such that $\dfrac{\bar{E}_2}{E_1} = \sqrt{\dfrac{2}{3}\dfrac{1-\eta}{1+2\eta}} = \tan\theta, \quad \theta \in \{0°, 9°, 18°, 30°, 45°, 65°, 90°\}$.

Finally, to be consistent with the isotropy hypothesis, numerical simulations have been performed on the most isotropic snow samples with respect to their elastic behavior from the snow database used in Wautier et al. (2015). With reference to the supporting information of the cited paper (Wautier et al., 2015), the name and the principal characteristics of each sample are recalled in Table 2. The porosities of the selected samples vary from 0.43 to 0.87, which covers almost the entire range of porosity of seasonal snow. Each sample presents similar correlation lengths (ℓ_1, ℓ_2, ℓ_3) (Löwe et al., 2013; Calonne et al., 2014) in the three space directions. All the simulations have been performed on volumes extracted from the 3D images sufficiently large to be considered as REV, as in Wautier et al. (2015).

Table 2. Names and principal characteristics of the six snow images of Wautier et al. (2015) reused in this study.

Sample name	Snow type	Dim (px)	Dim (mm)	Resolution (μm/px)	Snow density (kg/m^3)	Porosity	Correlation lengths (ℓ_1, ℓ_2, ℓ_3) (μm)	f	c
PP_123kg_600	PP	600	2.95	4.91	123.31	0.87	(64, 64, 65)	144.2	622.1
RG_172kg_600	RG	600	2.95	4.91	172.74	0.81	(92, 94, 97)	57.6	273.6
RG_256kg_512	RG	512	2.51	4.91	256.28	0.72	(113, 111, 110)	10.3	51.7
RG_1600	RG	600	4.46	7.43	330.13	0.64	(117, 111, 108)	4.7	24.2
RG_430kg_651	RG	651	5.61	8.61	430.59	0.53	(83, 82, 81)	1.9	12.0
MF_522kg_542	MF	542	5.42	10.00	522.31	0.43	(138, 134, 133)	0.6	5.1

3 Post-processing procedure: from macroscopic stress response to a homogenized model for snow visco-plasticity

From the homogenization procedure presented in the previous section, the time response of a given isotropic snow sample is recovered for the seven loading directions in the plane of the strain invariants $(E_1, \bar{E}_2)$ given by the equation (21). In order to deduce the overall viscous behavior of the snow considered from these few tests, a post-processing procedure consisting in basically three steps is proposed and summarized in Figure 2.

3.1 Extracting the viscous response (step a)

Because snow is locally modeled as an elasto-visco-plastic material in Abaqus (see subsection 2.1), the macroscopic time response $\boldsymbol{\Sigma}(t) = \dfrac{1}{|V|}\int_V \boldsymbol{\sigma}(\boldsymbol{x})\,\mathrm{d}V$ deduced from numerical simulations is composed of an elastic and a viscous part. The typical mechanical response of a snow sample to a constant strain rate is illustrated on Figure 3 for the snow sample *RG_1600* (Table 2) under a strain rate characterized by a loading angle $\theta = 65°$ (equation (21)). In order to reckon the influence of the elastic constitutive behavior on the overall mechanical response, the time response of the two first stress invariants S_1 and $\bar{S}_2$ is plotted for two different Young's moduli. In both cases, the initial mechanical response of the sample is driven by the elastic properties with a sharp increase in S_1 and $\bar{S}_2$ proportional to the Young's modulus under consideration (Figure 3).

The Cryosphere Discuss., doi:10.5194/tc-2016-272, 2016
Manuscript under review for journal The Cryosphere
Published: 5 December 2016

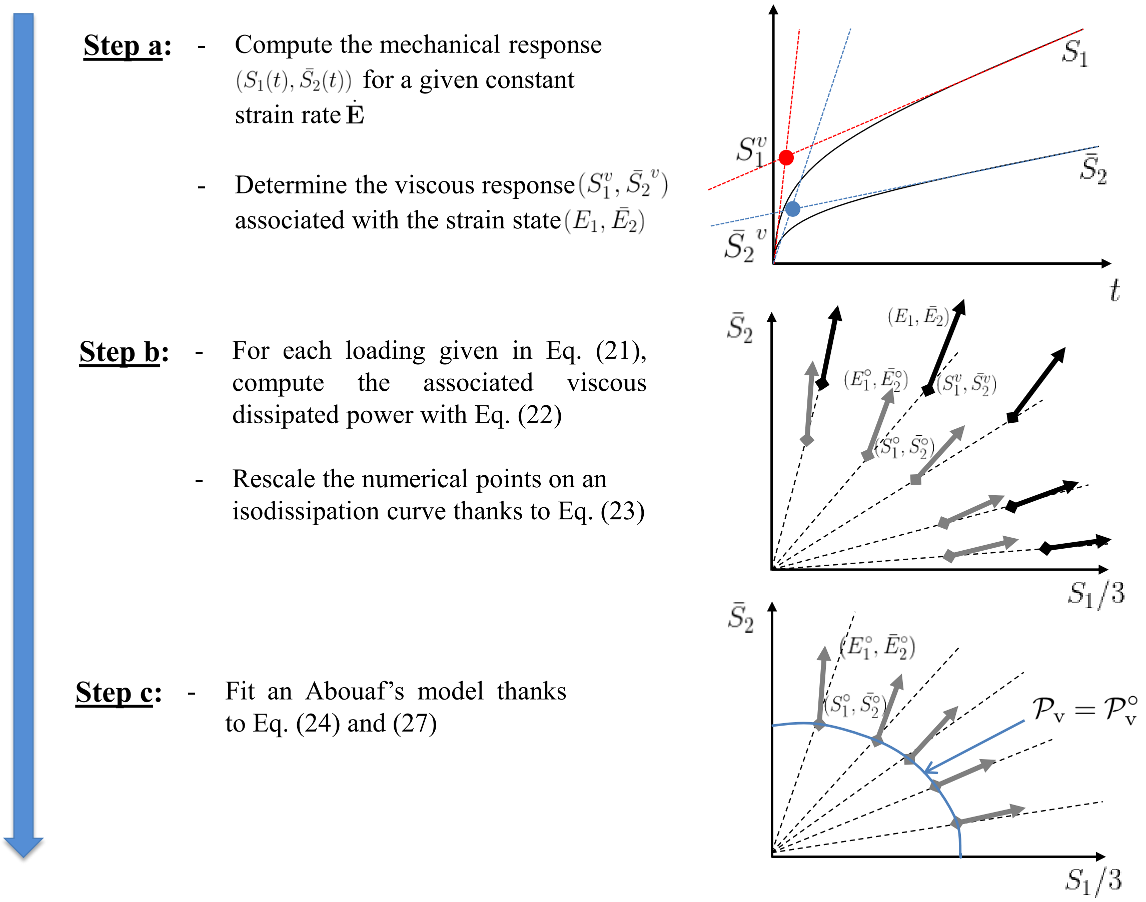

Step a: - Compute the mechanical response $(S_1(t), \bar{S}_2(t))$ for a given constant strain rate $\dot{\mathbf{E}}$

- Determine the viscous response $(S_1^v, \bar{S}_2{}^v)$ associated with the strain state $(E_1, \bar{E}_2)$

Step b: - For each loading given in Eq. (21), compute the associated viscous dissipated power with Eq. (22)

- Rescale the numerical points on an isodissipation curve thanks to Eq. (23)

Step c: - Fit an Abouaf's model thanks to Eq. (24) and (27)

Figure 2. Three-step post-processing procedure used in order to formulate a homogenized viscous constitutive equation.

Then a transient regime is observed followed by a permanent one in which the mechanical response is mainly driven by the viscoplastic behavior of ice. In the case where the ice viscosity is activated everywhere in the ice skeleton, the macroscopic stress $\mathbf{\Sigma}(t)$ should stabilize around a constant value according to equation (2) and to the fact that the strain rate is taken constant on average (see equation (21)). However, both stress invariants S_1 and $\bar{S}_2$ follow a non horizontal linear asymptote which slope is proportional to the Young's modulus value. Indeed, when E is increased by a factor 2, the slope of the linear asymptote is multiplied accordingly (Figure 3).

In order to extract the viscous component of the stress in the permanent regime, the initial an final asymptotes are plotted in Figure 3. Irrespective of the used Young's modulus values, their intersection points are characterized by very similar stress levels S_1 and $\bar{S}_2$. As a result, these values (noted S_1^v and $\bar{S}_2^v$ afterwards) characterize the macroscopic viscous response of the snow sample and are systematically used in the rest of this paper as the snow viscous homogeneous response to a given imposed constant macroscopic strain rate. The top graph in Figure 2 illustrates this step of the post-processing procedure.

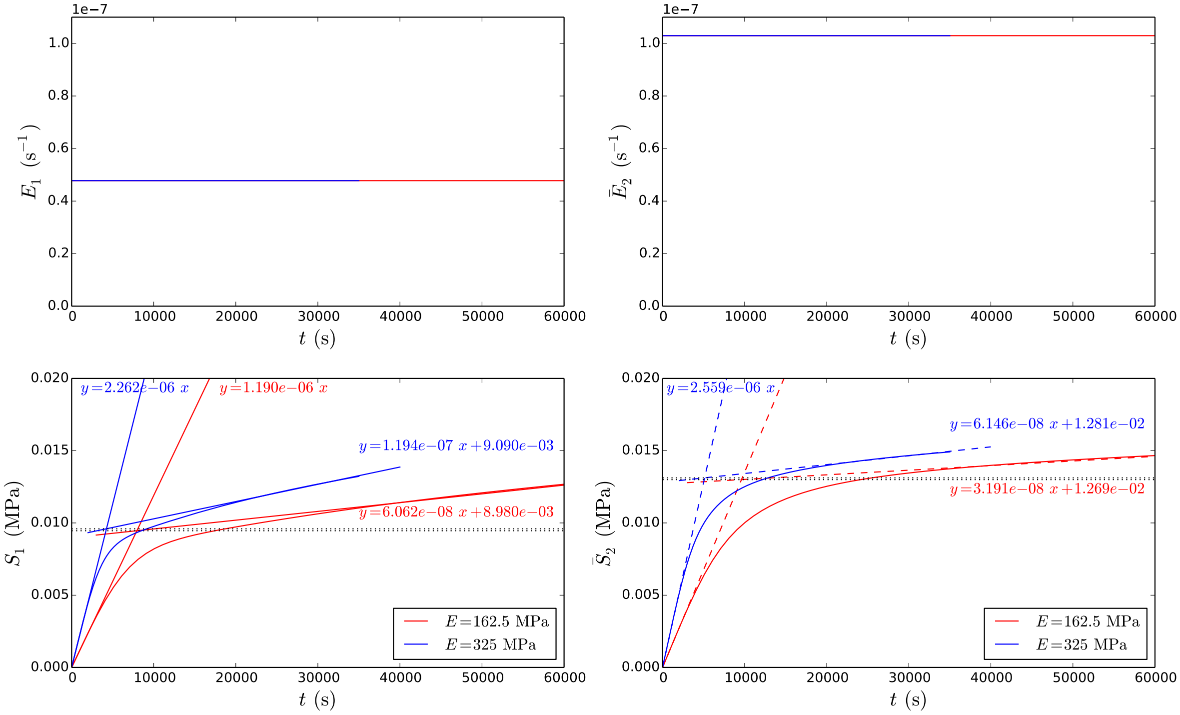

Figure 3. Strain rate (top) and stress (bottom) time responses of the sample *RG_1600* (see Table 2) under a strain loading characterized by $\theta = 65°$ in equation (21). Two Young's moduli are used and the resulting time responses are compared.

3.2 Computing isodissipation curves (step b)

For a given snow sample of porosity ϕ and for each applied loading path (21), the macroscopic volumetric mechanical dissipation $\mathcal{P}_{\rm v}$ (20) is computed as

$$\mathcal{P}_{\rm v} = \frac{1}{3} E_1 . S_1^v + \bar{E}_2 . \bar{S}_2^v, \tag{22}$$

where S_1^v and $\bar{S}_2^v$ are the characteristic stress invariants obtained in the first step of the post-processing process (Figure 2). Each loading path leads to different values of $\mathcal{P}_{\rm v}$. However, iso-mechanical dissipation points in the plane $(S_1/3, \bar{S}_2)$ can be recovered thanks to the homogeneity property (11). Given an arbitrary value of $\mathcal{P}_{\rm v}^\circ = 1$ Pa.s^{-1}, the corresponding macroscopic strain and stress invariants are computed as

$$(E_1^\circ, \bar{E}_2^\circ) = \left(\frac{\mathcal{P}_{\rm v}^\circ}{\mathcal{P}_{\rm v}}\right)^{n/(n+1)} (E_1, \bar{E}_2), \quad \text{and} \quad (S_1^\circ, \bar{S}_2^\circ) = \left(\frac{\mathcal{P}_{\rm v}^\circ}{\mathcal{P}_{\rm v}}\right)^{1/(n+1)} (S_1^v, \bar{S}_2^v). \tag{23}$$

Thanks to this rescaling, the seven homogenization tests (21) enable the description of an isodissipation curve in the plane of the stress invariants $(S_1/3, \bar{S}_2)$ as illustrated in Figure 2 (step b). For each point $(S_1^\circ/3, \bar{S}_2^\circ)$ on this graph, the associated flow vector $(E_1^\circ, \bar{E}_2^\circ)$ is plotted. The viscous dissipated power is thus simply equivalent to the scalar product $\left(S_1^\circ/3, \bar{S}_2^\circ\right) \cdot \left(E_1^\circ, \bar{E}_2^\circ\right)$.

3.3 Abouaf's model (step c)

Within the framework presented in section 2.2, Abouaf (1985) has suggested to use the macroscopic equivalent stress proposed by Green (1972) to describe the viscoplastic behavior of metal powders at high temperatures. This macroscopic equivalent stress $\Sigma_{\text{eq}}(\mathbf{\Sigma})$ is written

$$\Sigma_{\text{eq}}(\mathbf{\Sigma}) = \Sigma_{\text{eq}}(S_1, \bar{S}_2, \phi) = \sqrt{f(\phi)\, S_1^2 + \frac{3}{2} c(\phi)\, \bar{S}_2^2}, \tag{24}$$

where $f(\phi)$ and $c(\phi)$ are two material functions which depend on snow porosity only. When $\phi = 0$, we have $f(\phi) = 0$ and $c(\phi) = 1$ in order to recover the equivalent viscous stress of the ice matrix (3): $\Sigma_{\text{eq}}(\mathbf{\Sigma}, \phi = 0) = \sigma_{\text{eq}}(\boldsymbol{\sigma})$. From the definition of the viscous strain in (13) together with the previous definition of the equivalent stress in (24), it can be shown that

$$\dot{\mathbf{E}}_v = A \Sigma_{\text{eq}}^{n-1} \left(f(\phi) S_1 \mathbf{I} + \frac{3}{2} c(\phi) \bar{\mathbf{\Sigma}} \right). \tag{25}$$

As a result, the corresponding macroscopic equivalent strain rate introduced in (20) reads

$$\dot{\text{E}}_{\text{eq}}(\dot{\mathbf{E}}_v) = \dot{\text{E}}_{\text{eq}}(E_1, \bar{E}_2, \phi) = \sqrt{\frac{E_1^2}{9 f(\phi)} + \frac{2}{3} \frac{\bar{E}_2^2}{c(\phi)}}. \tag{26}$$

For a given porosity ϕ, the combination of (24) and (20) provides an implicit definition of $f(\phi)$ and $c(\phi)$ such that, for all $(S_1, \bar{S}_2)$

$$\Sigma_{\text{eq}}(S_1, \bar{S}_2, \phi) \; = \; \sqrt{f(\phi)\, S_1^2 + \frac{3}{2} c(\phi)\, \bar{S}_2^2} \; = \; \left(\frac{\mathcal{P}_{\text{v}}^\circ}{A} \right)^{1/(n+1)}. \tag{27}$$

In practise, the optimal values for $f(\phi)$ and $c(\phi)$ are obtained by minimizing the quadratic error between the model and the numerical points.

4 Results and discussion

The homogenization and the post-processing procedure presented in the previous sections are applied to six isotropic snow samples of various densities chosen in the same database as Wautier et al. (2015) and already introduced in Table 2. In Figure 4, the seven points $(S_1^\circ/3, \bar{S}_2^\circ)$ corresponding to the strain rates of equation (21) are represented for these six snow samples in the plane of the two first stress invariants. The corresponding strain flow vectors $(E_1^\circ, \bar{E}_2^\circ)$ are shown by solid arrows and the isodissipation curves corresponding to the fitted Abouaf model are represented by solid lines. The optimal values for f and c obtained for each snow type are presented on Figure 4 and reported in Table 2. It should be underlined here that each isodissipation curve is typical of a given snow characterized by its density and thus each curve is also an iso-density curve.

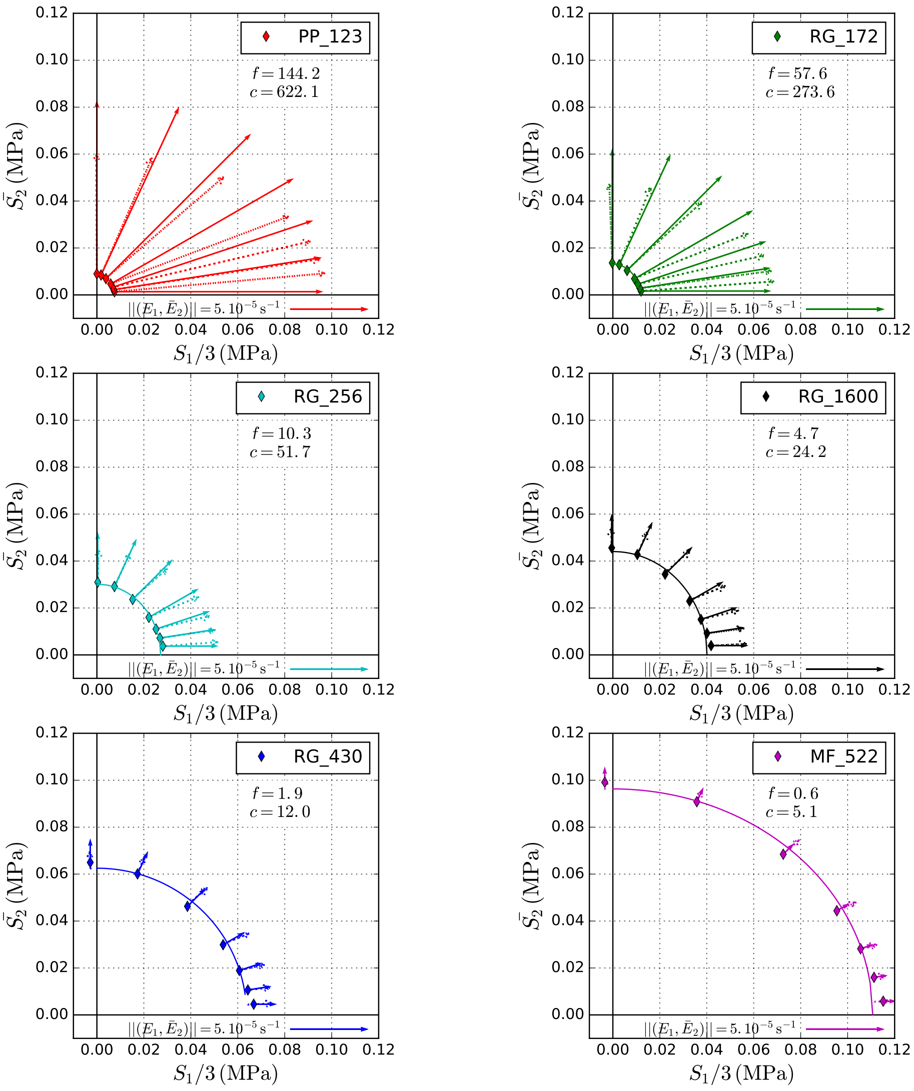

Figure 4. Isodissipation curves in the plane of the stress invariants $(S_1, \bar{S}_2)$ corresponding to an arbitrary dissipated power $\mathcal{P}_{\mathrm{v}}^{\circ}$ for the six snow samples of Table 2 in increasing density order. The associated strain flow vectors $(E_1, \bar{E}_2)$ are represented by solid arrows. Abouaf models are fitted to the numerical points (solid lines) and theoretical values of strain flow vectors are shown (dashed arrows). Parameters f and c of the fits are shown on the graphs and summarized in Table 2.

4.1 Isodissipation curves for different snow samples

The comparison between the simulated points and the Abouaf's model shows overall good agreement in terms of stress prediction even if a systematic slight deviation is observed between the model and the simulated points for the highest S_1 values. It should also be noticed that the stress state corresponding to an isotropic strain rate ($\bar{E}_2 = 0$) is not completely isotropic ($\bar{S_2} \neq 0$). This feature cannot be captured by the Abouaf modeling, which assumes a perfect isotropic behavior of the material. Even if the snow samples used in this study were selected as isotropic as possible, a slight anisotropy should account for the observed residual deviatoric stress component existing under an isotropic strain loading.

As already mentioned in section 2.2, the viscous behavior of snow should be insensitive to the sign of $\mathbf{\Sigma}$ as the ice matrix behave exactly the same in tension and in compression. In the stress space $(S_1/3, \bar{S_2})$, this results in the symmetry of the isodissipation curves with respect to the axis $S_1/3 = 0$. Provided that the isodissipation curves are smooth, their tangent for $S_1/3 = 0$ is horizontal which is respected in Figure 4. It must be mentioned that when snow is subjected to large strain levels, geometrical effects will introduce non linear effects and the mechanical response in tension will differ from the one in compression. These effects can also be investigated using the same homogenization procedure.

4.2 Density dependence of the isodissipation curves

As the snow density increases, the isodissipation curves tend to expand, and conversely the flow vectors tends to get smaller. In terms of physics, this means that the denser the snow, the smaller the applied strain rate in order to dissipate the same level of viscous power. In the meantime the applied stress should be increased. This is consistent with the fact that fresh snow tends to get denser more rapidly than already compacted snow under the same imposed loading.

The density dependence of the snow viscous behavior is fully described by the evolution of $f(\phi)$ and $c(\phi)$ with respect to the snow compacity ($\rho_{\text{snow}}/\rho_{\text{ice}} = 1-\phi$) represented in Figure 5. As the snow density decreases in Figure 5, the parameter values increase, which is consistent with the implicit definition of the isodissipation curves in equation (24). For a given equivalent stress Σ_{eq}, higher values for f and c will result in lower stress invariants S_1 and $\bar{S_2}$ as observed in Figure 4.

As classically done for metal powders (Geindreau et al., 1999b), some phenomenological fits can be proposed for f and c. In order to account for the change in the porosity range between metal powders and snow, the compacity limit value of 0.57 introduced in Table II in Geindreau et al. (1999b) is set equal to zero. As a result, the general form of the proposed fits is written

$$\left\{ \begin{array}{rcl} f(\phi) & = & a\left(\dfrac{\phi}{1-\phi}\right)^p \\ c(\phi) & = & 1+b\left(\dfrac{\phi}{1-\phi}\right)^q \end{array} \right. , \quad (a,b,p,q) \in \mathbb{R}^4. \tag{28}$$

The above fits respect the theoretical values $f(0) = 0$ and $c(0) = 1$ already mentioned in section 3.3. For a highly porous snow ($\phi \to 1$), an infinitely small stress level would be needed in order to produce a high viscous dissipation. This is consistent with the infinitely high values for f and c proposed by the above phenomenological fits (28). These fits allow a good description of the numerical points resulting from the homogenization of the six snow samples (Table 2) and are represented by solid

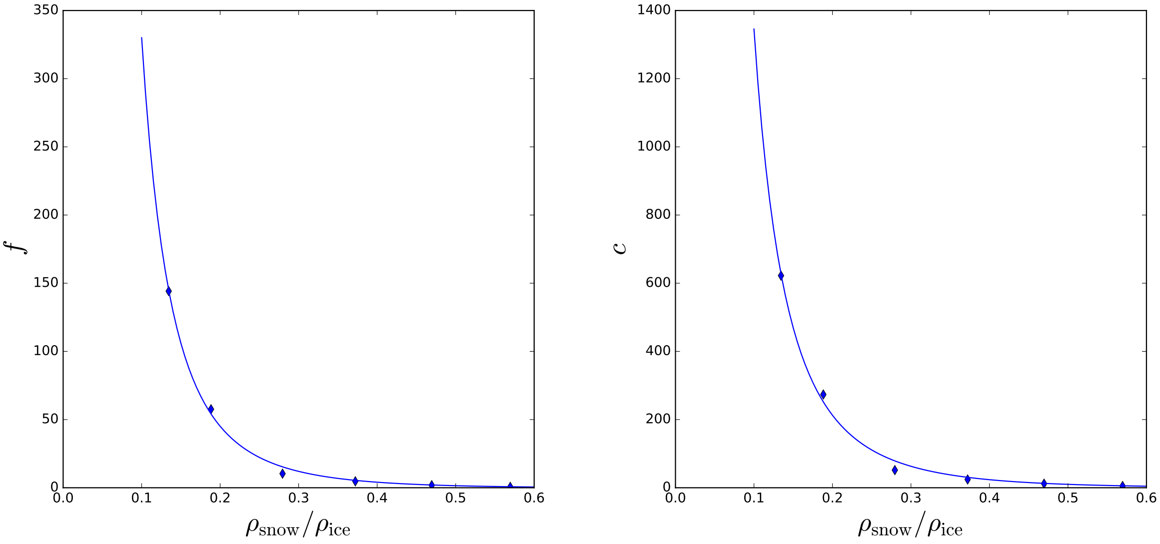

Figure 5. Evolution of the fitted Abouaf coefficients f and c with respect to the snow compacity (diamond points). Phenomenological fits as proposed in equation (28) are shown (solid lines).

Table 3. Optimal parameters chosen for the phenomenological fits (28).

Parameters	Values
a	1.50
p	2.45
b	8.97
q	2.28

lines in Figure 5. As a result, they may stand for a general formulation for the viscous isotropic behavior of snow according to its porosity through the four parameters (a,b,p,q) given in Table 3. Let us remark that the parameters a and b are close to the ones obtained for metal powders by Geindreau et al. (1999b). However, the exponents corresponding to the snow case are approximately twice bigger, which is linked to a more pronounced dependence on the porosity for very porous materials.

Another interesting feature which can be highlighted in Figure 4 is the fact that the isodissipation curves are closed for all the snow samples under consideration. This contrasts with the shape of ice isodissipation curves in the plane $(S_1/3, \bar{S}_2)$ which are represented by horizontal straight lines. Indeed, the corresponding viscous power doesn't depend on S_1 since the constitutive equation (2) for ice only involves the deviatoric stress $\overline{\boldsymbol{\sigma}}$. The ability of snow to dissipate some energy even under an isotropic loading ($\bar{S}_2 = 0$) is due to its porosity. Indeed, even under this type of macroscopic loading conditions, some regions of the snow microstructure experience a non zero deviatoric loading, which activates locally the viscous behavior of ice. Even if this deviatoric loading vanishes on average, the mean viscous dissipated power only piles up, which results in closed isodissipation

The Cryosphere Discuss., doi:10.5194/tc-2016-272, 2016
Manuscript under review for journal The Cryosphere
Published: 5 December 2016

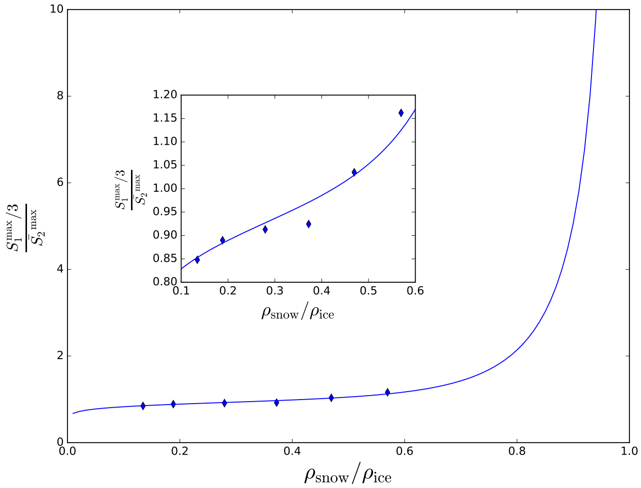

Figure 6. Aspect ratios of the fitted Abouaf models with respect to the snow compacity for each couple (f, c) recalled in Table 2 (diamond points) and for the phenomenological fits proposed in (28) (solid line).

curves. Their shapes provide information about the ability of an isotropic macroscopic loading to locally activate the ice viscous behavior. Based on the Abouaf formulation (24), the ratio between the maximum isotropic stress $S_1^{\max}/3$ and the maximum deviatoric stress $\bar{S}_2{}^{\max}$ can be expressed for each sample as

$$\frac{(S_1^{\max}/3)}{\bar{S}_2{}^{\max}} = \sqrt{\frac{c}{6f}}. \tag{29}$$

As snow is always submitted to a mechanical loading which can be decomposed into a deviatoric part and an isotropic part, this ratio provides a measure of the relative contribution of the isotopic part of the mechanical loading in the activation of the ice viscosity. The bigger this ratio, the smaller the activation degree. The evolution of this ratio is plotted in Figure 6 as a function of the snow compacity. The diamond points are computed using the values for f and c presented in Table 2 and the solid line is computed using the two phenomenological fits proposed in (28). The increase in this ratio with snow density highlights the fact that deviatoric fluctuations get smaller under isotropic loading conditions as snow gets denser. In other words, the ice viscosity is more difficult to activate for dense snow than for fresh snow. The divergence of the solid line around 1 corresponds to the limit case of ice where $S_1^{\max}$ becomes infinite as predicted by (3).

4.3 Normality rule

The proposed macroscopic modeling is formulated within the framework of associated viscoplasticity. In other words, the flow direction $\dot{\mathbf{E}}$ is by construction supposed to be orthogonal to the isodissipation curves (see equation (13)). In the space composed of the two first stress and strain invariants' planes, for an isodissipation curve corresponding to Σ_{eq}, this normality is written

$$\begin{pmatrix} E_1 \\ \bar{E}_2 \end{pmatrix} \propto \begin{pmatrix} \dfrac{3\partial\Sigma_{\text{eq}}}{\partial S_1} \\ \dfrac{\partial\Sigma_{\text{eq}}}{\partial \bar{S}_2} \end{pmatrix}. \tag{30}$$

In the case of the Abouaf's model (see equation (24)), the theoretical values of the strain flow vectors associated to the seven points in Figure 4 is written

$$\begin{pmatrix} E_1 \\ \bar{E}_2 \end{pmatrix} = A\Sigma_{\text{eq}}^{n-1} \begin{pmatrix} 3f(\phi)\,S_1 \\ \frac{3}{2}c(\phi)\,\bar{S}_2 \end{pmatrix}. \tag{31}$$

In Figure 4, the theoretical values of the strain flow vectors are represented by dashed arrows for the radial projections of the numerical points on the Abouaf fits. The overall comparison with their numerical counterparts represented by solid arrows is quite satisfactory, especially for the densest snows. However, concerning the flow direction, the Abouaf's model tends to over-predict the strain deviatoric component for high deviatoric stresses $\bar{S}_2$ and to under-predict the strain deviatoric component for low deviatoric stresses except for the direction $\theta = 0°$. In terms of magnitude, the Abouaf's model tends to under-predict the intensity of the flow for deviatoric loading.

The observed difference between theoretical and numerical flow vectors actually results from the slight misfit between the Abouaf models and the numerical points, which is amplified by the radial projection procedure used in order to compute the theoretical flow vectors. Moreover, the validity of normality rule tends to get less accurate as the porosity of the material increases. A similar trend has been already observed in the case of power law fluid flow through porous media (Orgéas et al., 2007). Overall, the Abouaf's model presented in section 3.3 provides a satisfactory modeling of the snow viscous behavior on the whole range of investigated densities.

5 Application to classical laboratory tests

In the case of isotropic snow microstructures, the homogenized constitutive viscous behavior developed in this paper can be summarized as follow:

$$\dot{\mathbf{E}}_v = \dot{\text{E}}_{\text{eq}} \frac{\partial \Sigma_{\text{eq}}}{\partial \mathbf{\Sigma}} = A\Sigma_{\text{eq}}^{n-1}\left(f(\phi)S_1\mathbf{I} + \frac{3}{2}c(\phi)\overline{\mathbf{\Sigma}}\right) \tag{32}$$

with

$$\Sigma_{\text{eq}}(S_1,\bar{S}_2,\phi) = \sqrt{f(\phi)\,S_1^2 + \frac{3}{2}c(\phi)\,\bar{S}_2^2}, \qquad \dot{\text{E}}_{\text{eq}}(E_1,\bar{E}_2,\phi) = \sqrt{\frac{E_1^2}{9f(\phi)} + \frac{2}{3}\frac{\bar{E}_2^2}{c(\phi)}}, \tag{33}$$

and

$$f(\phi) = a\left(\frac{\phi}{1-\phi}\right)^p, \qquad c(\phi) = 1 + b\left(\frac{\phi}{1-\phi}\right)^q \tag{34}$$

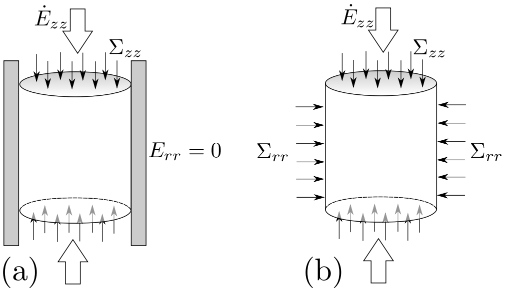

Figure 7. Oedometric compression test (a) and triaxial compression test (b).

where $n = 4.5$ and $A = 1.5 \times 10^{-3}$ MPa$^{-4.5}$.s^{-1} account for the ice viscosity and $a = 1.5$, $p = 2.45$, $b = 8.97$ and $q = 2.28$ account for the snow porosity.

In the following, the mechanical responses of the proposed model are analyzed and compared in the case of classical laboratory tests (Figure 7). In this figure the situation (a) corresponds to the oedometric compression test in which the radial deformation E_{rr} of the snow sample is prevented. The snow mechanical response is then characterized by the relationship between the axial stress Σ_{zz} and the axial strain rate $\dot{E}_{zz}$. In Figure 7, the situation (b) corresponds to the general triaxial compression test in which the radial stress Σ_{rr} is prescribed and kept constant. From this general setting, two particular cases can be studied: the uniaxial compression test with $\Sigma_{rr} = 0$ and the isotropic compression test with $\Sigma_{zz} = \Sigma_{rr}$. In all this section, the classical soil mechanics convention is adopted, i.e. compression stresses are positive, and the elasticity of snow is neglected.

5.1 Oedometric compression test

As the snow samples are often extracted from the snowpack thanks to hollow cylinders, the oedometric compression test is one of the most convenient mechanical laboratory test to perform on snow. Under the lateral constraint $E_{rr} = 0$, we have:

$$\dot{\boldsymbol{E}} = \begin{pmatrix} 0 & 0 & 0 \\ 0 & 0 & 0 \\ 0 & 0 & \dot{E}_{zz} \end{pmatrix}, \qquad \boldsymbol{\Sigma} = \begin{pmatrix} \Sigma_{rr} & 0 & 0 \\ 0 & \Sigma_{rr} & 0 \\ 0 & 0 & \Sigma_{zz} \end{pmatrix}, \quad \text{with } \Sigma_{zz} \geq \Sigma_{rr}. \tag{35}$$

As a result, the two first strain rate and stress invariants are written

$$E_1 = \dot{E}_{zz}, \qquad \bar{E}_2 = \sqrt{\frac{2}{3}}\dot{E}_{zz}, \qquad S_1 = 2\Sigma_{rr} + \Sigma_{zz}, \qquad \bar{S}_2 = \sqrt{\frac{2}{3}}(\Sigma_{zz} - \Sigma_{rr}). \tag{36}$$

In this particular case, from (32) and (33) it can be shown that the lateral constraint $E_{rr} = 0$ implies that:

$$\frac{\Sigma_{rr}}{\Sigma_{zz}} = \frac{c(\phi) - 2f(\phi)}{c(\phi) + 4f(\phi)}, \tag{37}$$

and consequently,

$$\Sigma_{\text{eq}} = \sqrt{\frac{9c(\phi)f(\phi)}{4f(\phi) + c(\phi)}}\Sigma_{zz}, \tag{38}$$

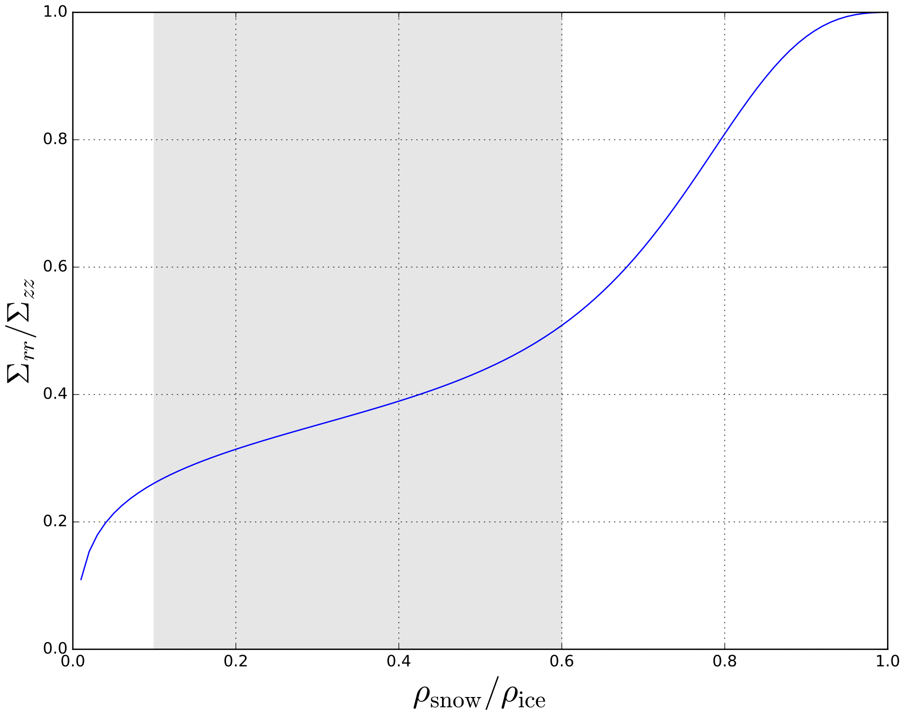

Figure 8. Evolution of the ratio between the lateral and axial stresses with respect to the snow compacity during any oedometric compression test. The compacity range for tipical snow samples is materialized by the grey zone.

and

$$\dot{E}_{zz} = A\left(\frac{9f(\phi)c(\phi)}{4f(\phi)+c(\phi)}\right)^{\frac{n+1}{2}} \Sigma_{zz}^n. \tag{39}$$

In oedometric experimental tests, the lateral pressure Σ_{rr} is not easily accessible and it is often tempting to neglect this pressure and interpret the oedometric compression test as a uniaxial compression test. The relation (37) can be used to assess the relative importance of the confining pressure with respect to the vertical stress. The evolution of this ratio with respect to the snow density is shown in Figure 8. It should be noticed that this ratio does not depend on the axial strain rate $\dot{E}_{zz}$. As expected, this ratio increases with increasing the snow density, and tends towards one for $\phi = 0$, due to the incompressiblity of the ice skeleton. The evolution of this ratio is similar to the one measured by Geindreau et al. (1999a) on metallic powders. In the whole range of snow compacities under consideration (materialized by the grey zone in Figure 8) the lateral pressure represents 30 to 50 % of the vertical stress and cannot be neglected in practice.

5.2 Triaxial compression test

During a triaxial test, the cylindric snow sample is submitted simultaneaously to an axial stress Σ_{zz} and a lateral confining pressure Σ_{rr}. Consequently, we have:

$$\dot{\boldsymbol{E}} = \begin{pmatrix} \dot{E}_{rr} & 0 & 0 \\ 0 & \dot{E}_{rr} & 0 \\ 0 & 0 & \dot{E}_{zz} \end{pmatrix}, \qquad \boldsymbol{\Sigma} = \begin{pmatrix} \Sigma_{rr} & 0 & 0 \\ 0 & \Sigma_{rr} & 0 \\ 0 & 0 & \Sigma_{zz} \end{pmatrix}. \tag{40}$$

As a result, the two first strain rate and stress invariants are written

$$E_1 = 2\dot{E}_{rr} + \dot{E}_{zz}, \qquad \bar{E}_2 = \sqrt{\frac{2}{3}}(\dot{E}_{zz} - \dot{E}_{rr}), \qquad S_1 = 2\Sigma_{rr} + \Sigma_{zz}, \qquad \bar{S}_2 = \sqrt{\frac{2}{3}}|\Sigma_{zz} - \Sigma_{rr}|. \tag{41}$$

In this particular case, from (32) and (33) it can be shown that:

$$\Sigma_{\text{eq}} = \sqrt{f(\phi)(2\Sigma_{rr} + \Sigma_{zz})^2 + c(\phi)(\Sigma_{zz} - \Sigma_{rr})^2}. \tag{42}$$

and

$$\begin{cases} \dot{E}_{rr} = A\Sigma_{\text{eq}}^{n-1}\left[\left(2f(\phi) + \frac{1}{2}c(\phi)\right)\Sigma_{rr} + \left(f(\phi) - \frac{1}{2}c(\phi)\right)\Sigma_{zz}\right] \\ \dot{E}_{zz} = A\Sigma_{\text{eq}}^{n-1}\left[\left(2f(\phi) - c(\phi)\right)\Sigma_{rr} + \left(f(\phi) + c(\phi)\right)\Sigma_{zz}\right] \end{cases}. \tag{43}$$

In the case of an uniaxial compression test, Σ_{rr} must be set to 0 in the above equations.

In order to compare the mechanical response of snow under various loadings (uniaxial, oedometric, isotropic and triaxial tests), Figure 9 presents the evolution of the snow densification rate given by $E_1 = \dot{\rho}_{\text{snow}}/\rho_{\text{snow}}$ with respect to the snow compacity when constant stresses are applied on the sample. As expected, this figure shows that:

- whatever the loading, the densification rate strongly decreases with increasing the snow density. In the investigated range, i.e. $\rho_{\text{snow}}/\rho_{\text{ice}} \in [0.1, 0.6]$, the densification rate decreases by 9 orders of magnitude from 10^{-1}s^{-1} to 10^{-10}s^{-1}.
- for a given snow density, the loading conditions influence strongly the densification rate. Typically, when $\Sigma_{zz} = 10$ kPa the densification rate decreases by nearly one order of magnitude if the confining pressure Σ_{rr} is reduced from 10 kPa (isotropic compression) to 0 kPa (uniaxial compression). On the contrary, when $\Sigma_{rr} = 10$ kPa, the densification rate increases by nearly one order of magnitude if the axial stress Σ_{zz} increases from 10 kPa (isotropic compression) to 20 kPa (triaxial compression). As expected, this last result shows the increase in the densification rate with the increase in the deviatoric stress (i.e. $\bar{S}_2$). Even if the lateral confining pressure cannot be neglected during oedometric test as highlighted in Figure 8, the oedometric compression test results in a similar densification rate as the uniaxial compression test for the same axial stress Σ_{zz}. Indeed, the vertical strain rate is lower for an oedometric compression than for a uniaxial one but the geometrical constraint imposed in the oedometric compression test prevents the snow sample from dilating, which is not the case for the uniaxial compression test. Overall the two effects cancel out. Finally, above the

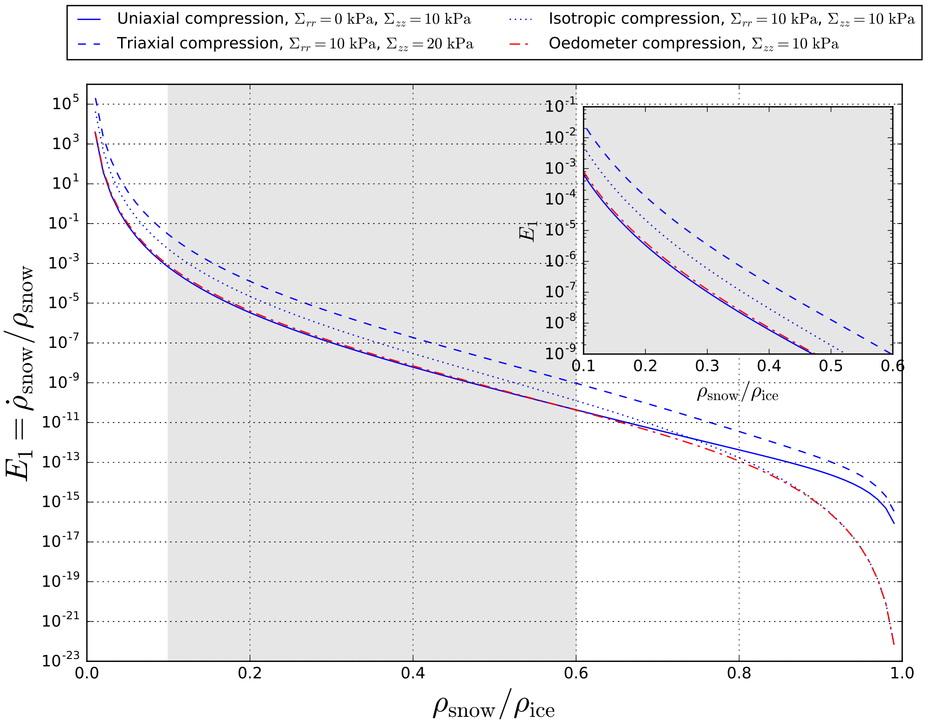

Figure 9. Predicted densification rate with respect to the snow compacity for four classical laboratory tests: an oedometric compression test (dash-dotted line), a uniaxial compression test (solid line), a triaxial compression test (dashed line) and an isotropic compression test (dotted line). The inset plot provides a zoom on the classical range of snow densities observed experimentally (grey background).

classical snow compacity range ($\rho_{\mathrm{snow}}/\rho_{\mathrm{ice}} \geq 0.6$), the densification rate dramatically decreases for the oedometric and isotropic compression tests due to the ice incompressibility. As already underlined in Figure 8 in this limit case, the oedometric compression test is equivalent to the isotropic compression one.

In practice, the strain rate is often imposed on the sample. The Figure 10 presents the evolution of the stress Σ_{zz} versus the snow compacity $\rho_{\mathrm{snow}}/\rho_{\mathrm{ice}} = 1 - \phi$ for two different values of strain rates $\dot{E}_{zz} \in \{10^{-7}; 10^{-5}\}$ s^{-1} and the different loading conditions (uniaxial, oedometric, isotropic and triaxial tests). This figure suggests the following comments:

- as expected, for a given strain rate, the stress Σ_{zz} increases with increasing snow density.
- for a given strain rate and a given density, the stress Σ_{zz} increases with increasing the lateral pressure Σ_{rr} around the sample.
- for a given snow density, the stress Σ_{zz} strongly increases with increasing strain rate, which is in accordance with the power law relationship.

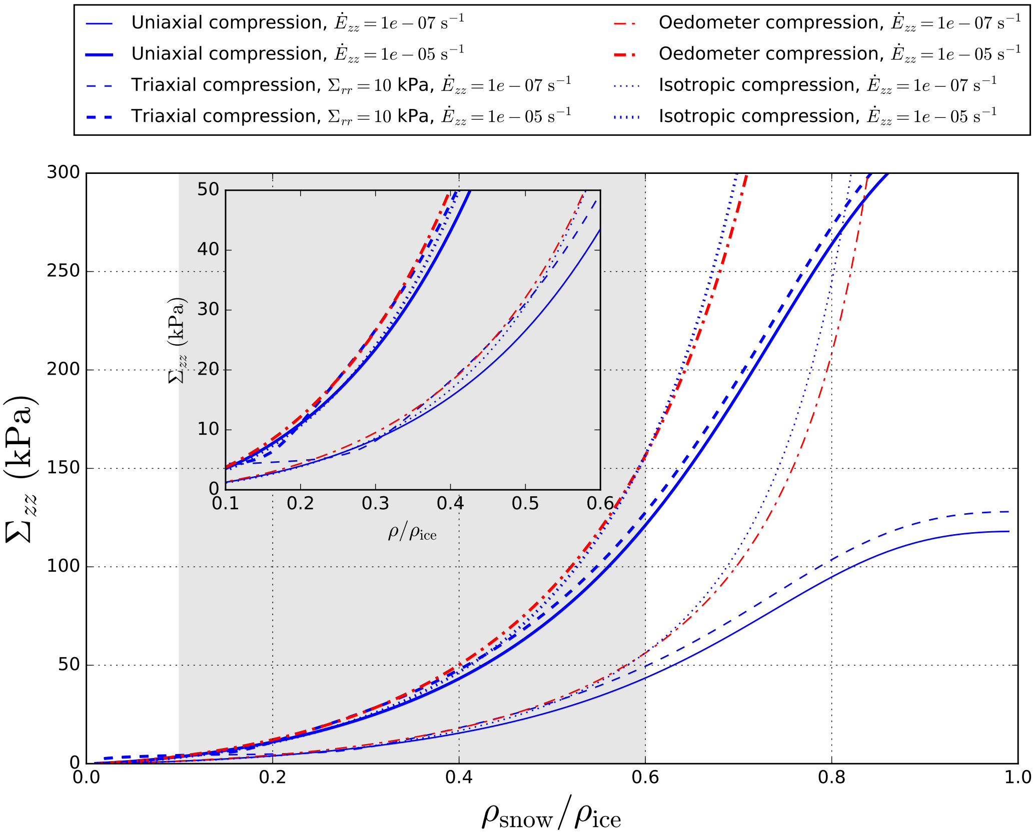

Figure 10. Predicted axial stress level with respect to the snow compacity for two imposed strain rates (line thickness) and for four classical laboratory tests: an oedometric compression test (dash-dotted line), a uniaxial compression test (solid line), a triaxial compression test (dashed line) and an isotropic compression test (dotted line). The inset plot provides a zoom on the classical range of snow densities observed experimentally (grey background).

- the ice viscoplastic behavior is recovered when $\rho_{\text{snow}}/\rho_{\text{ice}}$ tends towards 1. For a given strain rate, the axial stress for a uniaxial or triaxial compression test tends towards a maximum value. By contrast, due to the incompressibility of ice, the axial stress Σ_{zz} tends towards $+\infty$.

In order to quantitatively compare the predictions of our model against the experimental results of Bartelt and von Moos (2000), we consider a snow of density $\rho_{\text{snow}} = 255$ kg.m^{-3} (corresponding to $\rho_{\text{snow}}/\rho_{\text{ice}} = 0.27$) subjected to a confining pressure of $\Sigma_{rr} = 2.5$ kPa and a strain rate of 2.2×10^{-5} s^{-1}. In this case, the axial stress predicted by our model is $\Sigma_{zz} = 22.8$ kPa, which is consistent with the experimental values obtained by Bartelt and von Moos (2000) around 30 kPa.

The Cryosphere Discuss., doi:10.5194/tc-2016-272, 2016
Manuscript under review for journal The Cryosphere
Published: 5 December 2016

Further comparison with Bartelt and von Moos (2000) can be achieved in the case of the uniaxial compression test ($\Sigma_{rr} = 0$). In this case, the axial stress simply reads

$$\Sigma_{zz}(\dot{E}_{zz},\phi) \;=\; \left(\frac{\dot{E}_{zz}}{A(f(\phi)+c(\phi))^{\frac{n+1}{2}}}\right)^{\frac{1}{n}}. \tag{44}$$

For a given strain rate, the mechanical response of snow can be compared to the one of ice as in Bartelt and von Moos (2000) by using the following parameter:

$$\alpha_\eta(\phi) \;=\; \frac{\Sigma_{zz}^{\text{snow}}}{(1-\phi)\Sigma_{zz}^{\text{ice}}} \;=\; \frac{\Sigma_{zz}(\dot{E}_{zz},\phi)}{(1-\phi)\Sigma_{zz}(\dot{E}_{zz},0)} \;=\; \frac{1}{1-\phi}\left(\frac{1}{f(\phi)+c(\phi)}\right)^{\frac{n+1}{2n}}. \tag{45}$$

This parameter compares the axial stress that a given snow sample can transmit ($\Sigma_{zz}^{\text{snow}}$) to a rough estimate of this stress given as a fraction of the axial stress transmitted in the case of ice ($(1-\phi)\Sigma_{zz}^{\text{ice}}$). In Figure 11, the above theoretical expression of $\alpha_\eta(\phi)$ is compared with the experimental fit $\alpha_\eta = 0.0028\ \exp(0.008\rho_{\text{ice}} * (1-\phi))$ proposed by Bartelt and von Moos (2000). As expected, $\alpha_\eta(\phi)$ increases with increasing snow density. By definition, $\alpha_\eta(\phi)$ should vary between 0 and 1. We can observe that the theoretical expression of $\alpha_\eta(\phi)$ is strictly greater than 1 for $\rho_{\text{snow}}/\rho_{\text{ice}} \in [0.8, 1]$, which is not physically reasonable. This feature results from the independent choices of the parameters a, b, p and q in the fitting procedure used in subsection 4.2. An implicit relation between these parameters could help in order to ensure that $\alpha_\eta(\phi)$ remains lower than 1 in the whole compacity range. Nevertheless, in the range of snow densities under consideration ($\rho_{\text{snow}}/\rho_{\text{ice}} \in [0.1, 0.6]$), α_η increases monotonously between roughly 0.1 and 0.6. This prediction is higher than the experimental fit proposed by Bartelt and von Moos (2000) (see Figure 11). But during the experiment, the macroscopic mechanical response probably results from both the viscous deformation of the ice skeleton and the rupture of ice bridges between snow grains after few percents of deformation. This feature is not taken into account in the present model and may explain the observed differences.

6 Conclusions

Despite the non-linearity of the ice viscous constitutive equation, the homogenization approach introduced by Wautier et al. (2015) is successfully adapted to the numerical homogenization of the snow viscous behavior. By contrast to the elastic case, the macroscopic stress response is not a linear function of the imposed macroscopic strain anymore. As a result, the macroscopic response of snow is investigated in terms of isodissipation curves in the planes of the two first strain rate and stress invariants. Thanks to a few selected loading paths, an Abouaf's model was fitted onto the numerical results. This formulation seems to be relevant to describe the snow viscoplastic behavior in the whole range of snow density under consideration, provided that the snow microstructure is isotropic. The influence of the snow density, i.e. the porosity, on the viscoplastic response of snow is described through two functions ($f(\phi)$ and $c(\phi)$, see (28)).

The robustness of this Abouaf formulation is tested for several isotropic snow samples covering the whole range of accessible densities. The fitted models proved to be able to account for the stress and strain rate levels as well as the viscous flow directions. In particular, the ability of snow to exhibit a viscous behavior even under isotropic strain loading is recovered. The scope of

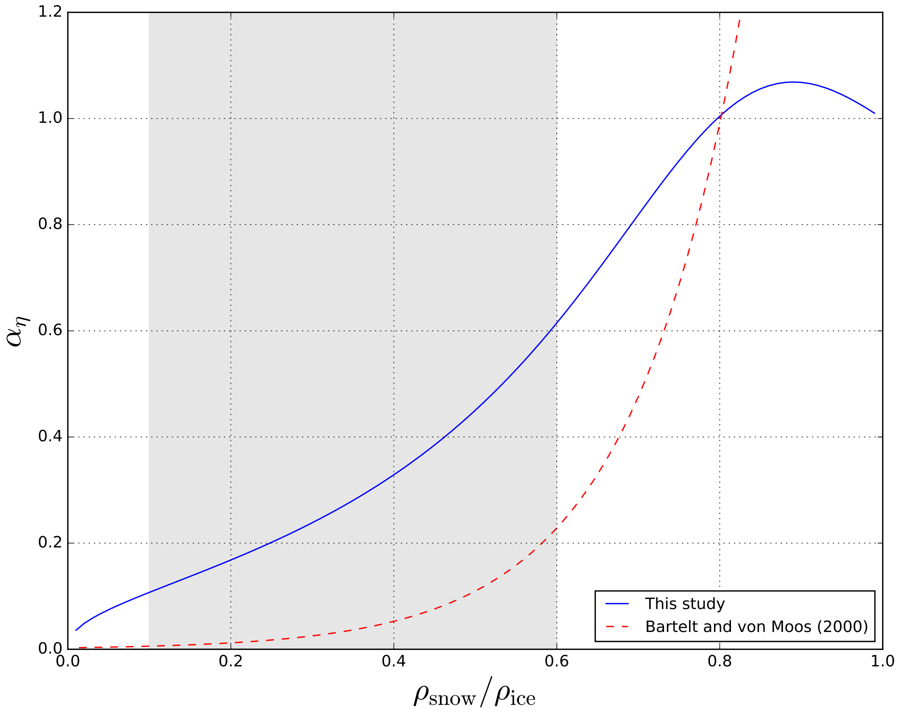

Figure 11. Comparison between our theoretical prediction for α_η (45) and the experimental fit proposed by Bartelt and von Moos (2000). The compacity range for snow samples under consideration is materialized by the grey zone.

application of the presented unified formulation is quite promising and could help improve the modeling of the densification of the snowpack in avalanche forecasting models.

The proposed homogenization model can be easily used to predict the viscous behavior of snow in classical laboratory tests as illustrated in the last section of this paper. However, the uncertainties made on our model parameters should be quantified through a sensitivity analysis, in order to reckon the ability of our homogenized law for snow viscosity to quantitatively recover the experimental results of Desrues et al. (1980); Bartelt and von Moos (2000); Moos et al. (2003); Scopozza and Bartelt (2003b).

Even though the porosity is known to have a very strong influence on the resulting homogenized properties of snow, it is also acknowledged that the very strong anisotropy of some snow microstructures cannot be neglected. The importance of this anisotropy was quantified within the framework of elasticity (Srivastava et al., 2010, 2016; Wautier et al., 2015) but additional work should be carried out in order to extend our homogenized visco-plastic formulation to anisotropic snow types.

Acknowledgements. We thank S. Lejeunes and S. Bourgeois from the LMA for sharing with us the code of their plugin Homtools and for helping us to use it in our scripts. Tomographic images have been acquired at ESRF (ID19) and 3SR Lab. CNRM-GAME/CEN is part of the LabEx OSUG@2020 (ANR10 LABX56). 3SR lab is part of the LabEx Tec 21 (Investissements d'Avenir - grant agreement ANR11 269 LABX0030).

References

Abouaf, M.: Modélisation de la compaction de poudres métalliques frittées, Ph.D. thesis, 1985.

Adams, E. E. and Walters, D. J.: Fine structure layering in radiation recrystallized snow, in: International Snow Science Workshop 2014 Proceedings, Banff, Canada, pp. 29–34, ISSW, 2014.

Auriault, J.-L., Bouvard, D., Dellis, C., and Lafer, M.: Modeling of hot compaction of metal powder by homogenization, Mech. Mater., 13, 247–275, 1992.

Auriault, J.-L., Royer, P., and Geindreau, C.: Filtration Law for Power Law Fluids in Anisotropic Media, Int. J. Eng. Sc., 40, 1151–1163, 2002.

Auriault, J.-L., Boutin, C., and Geindreau, C.: Homogenization of coupled phenomena in heterogenous media, vol. 149, John Wiley & Sons, 2010.

Bartelt, P. and von Moos, M.: Triaxial tests to determine a microstructure-based snow viscosity law, Annals of Glaciology, 31, 457–462, 2000.

Brzoska, J.-B., Coléou, C., Lesaffre, B., Borel, S., Brissaud, O., Ludwig, W., Boller, E., and Baruchel, J.: 3D visualization of snow samples by microtomography at low temperature, ESRF Newsletter, 32, 22–23, 1999.

Calonne, N., Geindreau, C., Flin, F., Morin, S., Lesaffre, B., Rolland du Roscoat, S., and Charrier, P.: 3-D image-based numerical computations of snow permeability: links to specific surface area, density, and microstructural anisotropy, The Cryosphere, 6, 939–951, doi:10.5194/tc-6-939-2012, 2012.

Calonne, N., Flin, F., Geindreau, C., Lesaffre, B., and Rolland du Roscoat, S.: Study of a temperature gradient metamorphism of snow from 3-D images: time evolution of microstructures, physical properties and their associated anisotropy, The Cryosphere, 8, 2255–2274, 2014.

Calonne, N., Flin, F., Lesaffre, B., Dufour, A., Roulle, J., Puglièse, P., Philip, A., Lahoucine, F., Geindreau, C., Panel, J.-M., Rolland du Roscoat, S., and Charrier, P.: CellDyM: A room temperature operating cryogenic cell for the dynamic monitoring of snow metamorphism by time-lapse X-ray microtomography, Geophysical Research Letters, 42, 3911–3918, doi:10.1002/2015GL063541, 2015.

Chandel, C., Srivastava, P. K., and Mahajan, P.: Micromechanical analysis of deformation of snow using X-ray tomography, Cold Regions Science and Technology, 101, 14–23, 2014.

Chen, S. and Baker, I.: Evolution of individual snowflakes during metamorphism, J. Geophys. Res., 115, D21114, doi:10.1029/2010JD014132, 2010.

Cresseri, S. and Jommi, C.: Snow as elastic viscoplastic bonded continuum: a modelling approach, Rivista Italiana Di Geotecnica, 4, 43–58, 2005.

Cresseri, S., Genna, F., and Jommi, C.: Numerical integration of an elastic-viscoplastic constitutive model for dry metamorphosed snow, Int. J. Num. Ana. Meth. Geomech, 34, 1271–1296, 2009.

Danas, K., Idiart, M., and Ponte Casteneda, P.: A homogenization-based constitutive model for isotropic viscoplastic porous media, Int. J. Solids and Struct., 45, 3392–3409, 2008.

Desrues, J., Darve, F., Flavigny, E., Navarre, J., and Taillefer, A.: An incremental formulation of constitutive equations for deposited snow, Journal of Glaciology, 25, 289–307, 1980.

Dormieux, L. and Bourgeois, E.: Introduction à la micromécanique des milieux poreux, Presses de l'École nationale des ponts et chaussées, 2002.

Fang, Q. and Boas, D. A.: Tetrahedral mesh generation from volumetric binary and grayscale images, in: Biomedical Imaging: From Nano to Macro, 2009. ISBI'09. IEEE International Symposium on, pp. 1142–1145, IEEE, http://iso2mesh.sourceforge.net/cgi-bin/index.cgi, 2009.

Fierz, C., Armstrong, R. L., Durand, Y., Etchevers, P., Greene, E., McClung, D. M., Nishimura, K., Satyawali, P. K., and Sokratov, S. A.: TheInternational Classificationi for Seasonal Snow on the Groun, UNESCO/IHP, 2009.

Flin, F. and Brzoska, J.-B.: The temperature-gradient metamorphism of snow: vapour diffusion model and application to tomographic images, Annals of Glaciology, 49, 17–21, 2008.

Fritzen, F., Forest, S., Bohlke, T., Kondo, D., and Kanit, T.: Computational homogenization of elasto-plastic porous metals, Int. J. of Plasticity, 29, 102–119, 2012.

Geindreau, C. and Auriault, J.-L.: Investigation of the Mechanical Behaviour of Alloys in the Semi-Solid State by Homogenization., Mechanics of Materials, 31, 535–551, 1999.

Geindreau, C., Bouvard, D., and Doremus, P.: Constitutive Behaviour of Metal Powder During Hot Forming. Part I : Experimental Investigation with Lead Powder as a Simulation Material, Eur. J. Mech. A/Solids, 18, 581–596, 1999a.

Geindreau, C., Bouvard, D., and Doremus, P.: Constitutive behaviour of metal powder during hot forming.: Part II: Unified viscoplastic modelling, European Journal of Mechanics-A/Solids, 18, 597–615, 1999b.

Green, R.: A plasticity theory for porous solids, International Journal of Mechanical Sciences, 14, 215–224, 1972.

Hagenmuller, P., Theile, T. C., and Schneebeli, M.: Numerical simulation of microstructural damage and tensile strength of snow, Geophys. Res. Lett., 41, 86–89, doi:10.1002/2013GL058078, 2014.

Hagenmuller, P., Chambon, G., and Naaim, M.: Microstructure-based modeling of snow mechanics: a discrete element approach, Cryosphere, 9, 1969–1982, 2015.

Kaempfer, T. U., Schneebeli, M., and Sokratov, S.: A microstructural approach to model heat transfer in snow, Geophysical Research Letters, 32, 2005.

Kanit, T., Forest, S., Galliet, I., Mounoury, V., and Jeulin, D.: Determination of the size of the representative volume element for random composites: statistical and numerical approach, International Journal of solids and structures, 40, 3647–3679, 2003.

Köchle, B. and Schneebeli, M.: Three-dimensional microstructure and numerical calculation of elastic properties of alpine snow with a focus on weak layers, Journal of Glaciology, 60, 705–713, 2014.

Lejeunes, S., Bourgeois, S., et al.: Une Toolbox Abaqus pour le calcul de propriétés effectives de milieux hétérogènes, in: 10e colloque national en calcul des structures, http://www.lma.cnrs-mrs.fr/spip.php?article171, 2011.

Lemaitre, J. and Chaboche, J.-L.: Mécanique des Matériaux Solides, Dunod, Paris, 1985.

Liu, I.: On Representations of Anisotropic Invariants, Int. J. Eng. Sci., 19, 1099–1109, 1982.

Löwe, H., Riche, F., and Schneebeli, M.: A general treatment of snow microstructure exemplified by an improved relation for thermal conductivity, The Cryosphere, 7, 1473–1480, doi:10.5194/tc-7-1473-2013, 2013.

Mellor, M.: A review of basic snow mechanics, US Army Cold Regions Research and Engineering Laboratory, 1974.

Moos, M. v., Bartelt, P. A., Zweidler, A., and Bleiker, E.: Triaxial tests on snow at low strain rate. Part I: Experimental device, Journal of Glaciology, 49, 81–90, 2003.

Narita, H.: An experimental study on tensile fracture of snow, Contributions from the institute of Low Temperature Science, 32, 1–37, 1984.

Navarre, J. P., Meyssonnier, J., and Vagnon, A.: 3D numerical model of snow deformation without failure and its application to cold room mechanical tests, Cold Regions Science and Technology, 50, 3–12, 2007.

Orgéas, L., Geindreau, C., Auriault, J.-L., and Bloch, J.-F.: Upscaling the flow of generalised Newtonian fluids through anisotropic porous media, Journal of Non-Newtonian Fluid Mechanics, 145, 15–29, 2007.

Pieritz, R. A., Brzoska, J.-B., Flin, F., Lesaffre, B., and Coléou, C.: From snow X-ray microtomograph raw volume data to micromechanics modeling: first results, Ann. Glaciol., 38, 52–58, doi:10.3189/172756404781815176, 2004.

Pinzer, B., Schneebeli, M., and Kaempfer, T.: Vapor flux and recrystallization during dry snow metamorphism under a steady temperature gradient as observed by time-lapse micro-tomography, The Cryosphere Discussions, 6, 1673–1714, 2012.

Salm, B.: Mechanical properties of snow, Rev. Geophys., 20, 1–19, 1982.

Schleef, S., Löwe, H., and Schneebeli, M.: Hot-pressure sintering of low-density snow analyzed by X-ray microtomography and in situ microcompression, Acta Materialia, 71, 185–194, 2014.

Schneebeli, M.: Numerical simulation of elastic stress in the microstructure of snow, Annals of Glaciology, 38, 339–342, 2004.

Schulson, E. M., Duval, P., et al.: Creep and fracture of ice, Cambridge University Press Cambridge, 2009.

Schweizer, J. and Camponovo, C.: The temperature dependence of the effective elastic shear modulus of snow, Cold Regions Science and Technology, 35, 55–64, 2002.

Scopozza, C. and Bartelt, P. A.: The influence of temeprature on the small strain viscous deformation mechanics of snow: comparison with polycrystalline ice, Annals of Glaciology, 37, 90–96, 2003a.

Scopozza, C. and Bartelt, P. A.: Triaxial tests on snow at low strain rate. Part II: Constitutive modelling, Journal of Glaciology, 49, 91–101, 2003b.

Shapiro, L. H., Johnson, J. B., Sturm, M., and Blaisdell, G. L.: Snow mechanics: review of the state of knowledge and applications, 1997.

Smith, G.: On Isotropic Functions of Symmetric Tensors Skew-Symmetric Tensors and Vectors, Int. J. Eng. Sci., 9, 899–916, 1971.

Srivastava, P., Mahajan, P., Satyawali, P., and Kumar, V.: Observation of temperature gradient metamorphism in snow by X-ray computed microtomography: measurement of microstructure parameters and simulation of linear elastic properties, Annals of Glaciology, 51, 73–82, 2010.

Srivastava, P. K., Chandel, C., Mahajan, P., and Pankaj, P.: Prediction of anisotropic elastic properties of snow from its microstructure, Cold Regions Science and Technology, 125, 85–100, 2016.

Suquet, P.: Overall potentials and extremal surfaces of power law or ideally plastic composites, Journal of the Mechanics and Physics of Solids, 41, 981–1002, 1993.

Theile, T., Lowe, H., Theile, T. C., and Schneebeli, M.: Simulating creep of snow based on microstructure and anisotropic deformation of ice, Acta Materialia, 59, 7104–7113, 2011.

Wang, X. and Baker, I.: Observation of the microstructural evolution of snow under uniaxial compression using X-ray computed microtomography, Journal of Geophysical Research: Atmospheres, 118, 12–371, 2013.

Wautier, A., Geindreau, C., and Flin, F.: Linking snow microstructure to its macroscopic elastic stiffness tensor: A numerical homogenization method and its application to 3-D images from X-ray tomography, Geophysical Research Letters, 42, 8031–8041, 2015.